

Omniscopes: Large Area Telescope Arrays with only $N \log N$ Computational Cost

Max Tegmark

Dept. of Physics & MIT Kavli Institute, Massachusetts Institute of Technology, Cambridge, MA 02139

Matias Zaldarriaga

Institute for Advanced Study, Einstein Drive, Princeton, NJ 08540, USA

(Dated: Submitted to *Phys. Rev. D* August 31 2009, revised June 9 2010, accepted August 7 2010)

We show that the class of antenna layouts for telescope arrays allowing cheap analysis hardware (with correlator cost scaling as $N \log N$ rather than N^2 with the number of antennas N) is encouragingly large, including not only previously discussed rectangular grids but also arbitrary hierarchies of such grids, with arbitrary rotations and shears at each level. We show that all correlations for such a 2D array with an n -level hierarchy can be efficiently computed via a Fast Fourier Transform in not 2 but $2n$ dimensions. This can allow major correlator cost reductions for science applications requiring exquisite sensitivity at widely separated angular scales, for example 21cm tomography (where short baselines are needed to probe the cosmological signal and long baselines are needed for point source removal), helping enable future 21cm experiments with thousands or millions of cheap dipole-like antennas. Such hierarchical grids combine the angular resolution advantage of traditional array layouts with the cost advantage of a rectangular Fast Fourier Transform Telescope. We also describe an algorithm for how a subclass of hierarchical arrays can efficiently use rotation synthesis to produce global sky maps with minimal noise and a well-characterized synthesized beam.

I. INTRODUCTION

There is now strong community interest in building more sensitive radio telescopes, stemming from diverse science opportunities that range from planets to pulsars, from black holes to cosmology [1]. However, greater sensitivity requires greater collecting area, which in turn increases cost. The cost for a steerable single-dish telescope grows faster than linearly with area, and becomes prohibitive beyond a certain point, which has bolstered interest in interferometers. Interferometer arrays can be made arbitrarily large, but for a generic array layout, the cost unfortunately grows quadratically with area asymptotically, eventually becoming financially unviable. The reason for this is that for an array of N antennas, all $N(N-1)/2 \propto N^2$ pairs of antennas need to be correlated to calculate the so-called visibilities which encode the sky image. Thus the cost of the hardware performing these computations scales as N^2 , dominating all other costs of the interferometer (which tend to grow linearly) for sufficiently large N . An array of $N \sim 10^6$ cheap dipole-style antennas has the potential to greatly improve constraints on dark matter, dark energy, inflation, reionization, *etc.* [2–7], and the N^2 -component of the cost starts dominating already around $N \sim 10^3$ [8].

To overcome this limitation, two cost-cutting approaches have emerged:

1. Partitioning the array into “tiles” of M antennas apiece, each treated as a single element as in [8–11]. This cuts the correlation cost from N^2 to $(N/M)^2$, at the price of reducing the sky area covered by a factor M . In other words, the time savings entirely come from throwing away available sky information and thus not needing to compute it.
2. Arranging the antennas into a rectangular grid that

can be correlated using Fast Fourier Transforms (FFTs) [12–18]. This reduces the computational cost from N^2 to $N \log_2 N$, but by lacking long baselines between antennas, a fully sampled square grid provides much lower resolution than a conventional sparse array.

The goal of the present paper is to explore what class of antenna layouts permit cheap ($N \log_2 N$) signal processing without throwing away any information. We will show that this class is encouragingly large, including not only the above-mentioned rectangular FFT grids, but also arbitrary hierarchies of such grids, such as the example shown in Figure 1. This opens up the possibility of getting the best of both worlds, combining affordable signal processing with baseline coverage tailored to specific scientific needs. We will refer to such an array that is effectively omnidirectional and omnichromatic as an *omniscopes*¹.

The computational savings of this type of arrays comes at a price. By construction, the array instantaneously measures a significantly smaller number of visibilities (of order N rather than N^2). As we will discuss later, this drawback can be compensated at least partially by sky

¹ If the electric field is digitized at set of antenna elements with broad primary beams (like those of the MWA [8], PAPER [10] or 21CMA [11], say) and these antennas are correlated individually rather than in tiles, then the instantaneous field-of-view will be much of the solid angle above the horizon, and the spectral coverage in principle covers a large fraction of the range from zero up to the Nyquist frequency, limited only by antenna and feed response, analog filtering requirements, *etc.* The designation “telescope” feels like a misnomer for such an instrument, since it is not zooming in on a distant object subtending a small fraction of the sky.

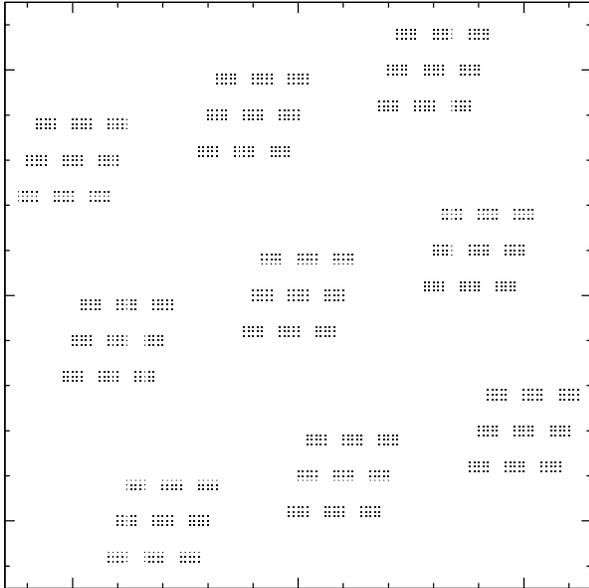


FIG. 1: Example of a 3-level hierarchy of antennas, with 5×3 blocks arranged in 3×3 blocks that are in turn placed in a 3×3 block. Note that the blocks at each level can be non-square (like at level 1), sheared (like at level 2) and rotated (like at level 3), in any combination. We show that this particular array can be efficiently correlated with a 6-dimensional FFT.

rotation. Furthermore, this reduced number of instantaneous visibilities implies an enormous redundancy: each visibility is independently measured by order N different antenna pairs, providing an opportunity for vastly improved calibration and systematics control.

The rest of this paper is organized as follows. In Section II, we describe our hypercube algorithm for analyzing arbitrary multi-level arrays in $N \log_2 N$ time. In Section III, we provide examples of how the sky can be probed with arrays in this class. We summarize our conclusions in Section IV. In Appendix A, we describe how multiple measurements from such arrays can be rapidly merged into sky maps of the full curved sky.

II. THE HYPERCUBE ALGORITHM

A. Background

For a modern introduction to radio astronomy, see *e.g.* [19]. A brief and self-contained description of how a rectangular array of N antennas can map essentially the whole sky above the horizon at $N \log_2 N$ computational cost can be found in [18], without using any of the approximations that are commonly used in radio astronomy. One arranges data from each antenna (at a given

frequency, say) in a rectangular array, and convolves this array with a parity-reversed copy of itself, obtaining an image of what radio astronomers refer to as “visibilities” in the “ uv plane”. Mathematically, this is equivalent to performing an FFT, computing its square modulus, and performing an inverse FFT. Each visibility is simply the correlation of signals from antennas separated by the corresponding distance vector (known as a baseline) summed over all pairs with the same separation. Such uv plane observations made at different times can then be combined to average down instrumental noise. For any given pointing, only a fraction of pixels in the uv plane will be measured, but Earth’s rotation can be exploited to fill in missing baselines. This final uv plane image is essentially the Fourier transform of the sky — [18] includes the complications of polarization and sky curvature.

B. Hierarchical grids

A more complicated sparse array layout such as the one in Figure 1 can of course be analyzed with this same formalism if the FFTs used for the correlation are performed on a square grid where each antenna falls in a single entry or pixel, but where many of the entries are empty. This would be as time consuming as analyzing a non-sparse (fully filled) grid, thus taking no advantage of the sparseness. In the example in Figure 1, this procedure would increase of the computational cost by a factor of ~ 8 , and this inefficiency factor would be much larger for arrays involving some very long baselines.

Fortunately, there is a much better way: simply arrange the data from Figure 1 in a 6-dimensional hypercube of dimensions $5 \times 3 \times 3 \times 3 \times 3 \times 3$, and perform the correlation in 6 dimensions using 6-dimensional FFTs. We prove below that this gives the exact same result, and this computation is clearly much faster: it scales as $N \log_2 N$ where N is not the total number of pixels in Figure 1, but only the number of pixels containing an antenna.

C. A warmup example

Before getting rigorous, let us consider the following simple toy example to clarify the situation. Suppose we have a simple one-dimensional array consisting of $N = 6$ antennas arranged in 2 groups of 3, located along the x -axis at positions $x_i = 1, 2, 3, 7, 8, 9$ in some units. The corresponding possible separations are all integers $-8 \leq \Delta x \leq 8$ except $\Delta x = \pm 3$. Suppose moreover that in some appropriate units, they happen to measure voltage values $f_i = 1, 2, 3, 4, 5, 6$. Arranging the voltages measured along the x -axis in a vector $\mathbf{f} = (1, 2, 3, 0, 0, 4, 5, 6)$, we now wish to compute the convolution of \mathbf{f} with its parity reversed version $\mathbf{f}^- = (6, 5, 4, 0, 0, 3, 2, 1)$ to obtain the visibility vector $\mathbf{g} \equiv \mathbf{f} \star \mathbf{f}^-$, where \star denotes convolu-

tion. This visibilities vector will contain the product of the voltages of antennas separated by a given distance, summed over all pairs with the same separation. For an n -dimensional vector \mathbf{f} , this convolution is defined by

$$g_i \equiv (\mathbf{f} \star \mathbf{f}^-)_i \equiv \sum_{j=\max\{1, i+1\}}^{\min\{n, i+n\}} f_j f_{j-i}, \quad (1)$$

where $i = -(n-1), \dots, n-1$ (i corresponds to differences between the integers $j = 1, \dots, n$).

There are now three equivalent ways in which we can compute this. The slowest of all would be to simply compute all the $N^2/2$ products and sum up the ones corresponding to the same separation. The other two rely on doing FFTs, in either a slower or a faster way. The slower would just perform a zero-padded FFT, squaring the result and inverse transforming. The result is

$$\begin{aligned} \mathbf{g} &= (1 \ 2 \ 3 \ 0 \ 0 \ 0 \ 4 \ 5 \ 6) \star (6 \ 5 \ 4 \ 0 \ 0 \ 0 \ 3 \ 2 \ 1) \\ &= (6 \ 17 \ 32 \ 23 \ 12 \ 0 \ 27 \ 58 \ 91 \ 58 \ 27 \ 0 \ 12 \ 23 \ 32 \ 17 \ 6). \end{aligned}$$

However, by instead arranging the measured data in a 2D array, we can obtain the same answer by performing a 2D convolution exploiting 2D FFTs:

$$\begin{pmatrix} 1 & 2 & 3 \\ 4 & 5 & 6 \end{pmatrix} \star \begin{pmatrix} 6 & 5 & 4 \\ 3 & 2 & 1 \end{pmatrix} = \begin{pmatrix} 6 & 17 & 32 & 23 & 12 \\ 27 & 58 & 91 & 58 & 27 \\ 12 & 23 & 32 & 17 & 6 \end{pmatrix}. \quad (2)$$

The latter is faster, since it eliminates all “multiply by zero” steps stemming from the sparseness of the 1D array. The sparser the array, the greater the speedup. Note that there are two copies of all but the middle number in the final convolution, which is effectively a palindrome. This is of course because the inputs are real-valued; by performing a real FFT, one avoids computing these numbers twice.

D. The general case

Let us now investigate why this trick works and generalize it. We define a hierarchical grid as a set of points of the form

$$\mathbf{r} = i_1 \mathbf{a}_1 + i_2 \mathbf{a}_2 + \dots, \quad (3)$$

where i_1, i_2, \dots are integers spanning some finite ranges and $\mathbf{a}_1, \mathbf{a}_2, \dots$ are vectors. We will be mainly interested in the case where these are 2-dimensional vectors, but our algorithm works for any dimensionality. We will insist that the integer ranges be such that each point \mathbf{r} in the grid corresponds to a unique set of integers. Our toy example above corresponds to the special case $\mathbf{a}_1 = (1, 0)$, $\mathbf{a}_2 = (6, 0)$, $i_1 = 1, 2, 3$ and $i_2 = 0, 1$. The 3-level hierarchical grid in Figure 1 corresponds to $\mathbf{a}_1 = (1, 0)$, $\mathbf{a}_2 = (8, 0)$, $\mathbf{a}_3 = (40, 10)$, $\mathbf{a}_4 = (0, 1)$, $\mathbf{a}_5 = (2, 8)$, $\mathbf{a}_6 = (-10, 40)$, $n_1 = 1, \dots, 5$ and n_2 through n_6 all ranging from 1 to 3.

Following the notation from Section II C above, we let $f_{\mathbf{r}}$ denote the voltage measured by the antenna at position \mathbf{r} (at some time, in some frequency band) and wish to compute the visibility map $\mathbf{g} \equiv \mathbf{f} \star \mathbf{f}^-$. Using equation (3) and the definition of convolution, we obtain

$$\begin{aligned} g_{\mathbf{r}} &= g_{\mathbf{j}+i_1 \mathbf{a}_1 + i_2 \mathbf{a}_2 + \dots} = \sum_{\mathbf{r}'} f_{\mathbf{r}'} f_{\mathbf{r}' - \mathbf{r}} = \\ &= \sum_{\mathbf{j}' i'_1 i'_2 \dots} f_{\mathbf{j}' + i'_1 \mathbf{a}_1 + i'_2 \mathbf{a}_2 + \dots} f_{(\mathbf{j}' + i'_1 \mathbf{a}_1 + i'_2 \mathbf{a}_2 + \dots) - (\mathbf{j} + i_1 \mathbf{a}_1 + i_2 \mathbf{a}_2 + \dots)} \\ &= \sum_{i'_1 i'_2 \dots} f_{i'_1 \mathbf{a}_1 + i'_2 \mathbf{a}_2 + \dots} f_{-\mathbf{j} + (i'_1 - i_1) \mathbf{a}_1 + (i'_2 - i_2) \mathbf{a}_2 + \dots} \end{aligned} \quad (4)$$

On the first line, we have included a residual vector $\mathbf{j} \equiv \mathbf{r} - (i_1 \mathbf{a}_1 + i_2 \mathbf{a}_2 + \dots)$ to allow for the fact that \mathbf{r} may not lie on the grid. We have introduced an analogous vector \mathbf{j}' on the second line to ensure that the sum runs over all \mathbf{r}' -values, not merely those in the grid. Since our measurements f vanish off the grid, we have $f_{\mathbf{j}' + i'_1 \mathbf{a}_1 + i'_2 \mathbf{a}_2 + \dots} = 0$ whenever $\mathbf{j}' \neq \mathbf{0}$, so that we can set $\mathbf{j}' = \mathbf{0}$ and sum only over i'_1, i'_2, \dots . Rearranging terms on the third line, we see that the second factor now vanishes whenever $\mathbf{j} \neq \mathbf{0}$, which means that $g_{\mathbf{r}}$ equals zero outside the grid and need only be computed on the grid. Defining $F_{i_1 i_2 \dots} \equiv f_{i_1 \mathbf{a}_1 + i_2 \mathbf{a}_2 + \dots}$ and $G_{i_1 i_2 \dots} \equiv g_{i_1 \mathbf{a}_1 + i_2 \mathbf{a}_2 + \dots}$, we can therefore rewrite equation (4) as

$$G_{i_1 i_2 \dots} = \sum_{i'_1 i'_2 \dots} F_{i'_1 i'_2} F_{(i'_1 - i_1), (i'_2 - i_2), \dots}, \quad (5)$$

which we recognize as simply a multidimensional convolution. Note that if an index of F runs from 1 to n , the corresponding index of G runs from $-(n-1)$ to $(n-1)$.

This result is very general: the proof assumes only that the mapping from \mathbf{r} to a set of integers is unique, so grid points are even allowed to be interleaved between different levels of the hierarchy as long as they never collide — consider for example $\mathbf{a}_1 = (5, 0)$, $\mathbf{a}_2 = (7, 0)$, $i_1 = 1, \dots, 4$ and $i_2 = 1, \dots, 4$. Moreover, the proof is readily generalized to the case where the components of \mathbf{r} are not integers or even rational numbers.

III. EXAMPLES

Because of the hypercube data analysis algorithm described above, the class of antenna layouts for affordable large-area radio telescope arrays is quite large. In this section, we illustrate the possibilities with some simple examples.

Figures 2-5 show four hierarchical grid omniscience layouts that we nickname “3-level” (Figure 2), “Blocks” (Figure 3), “Plank” (Figure 4) and “Strips” (Figure 5). In all cases, separations are in units of the minimum spacing between antennas, which in our examples is 1 meter. For comparison, we have also analyzed four non-hierarchical layouts for which the computational cost

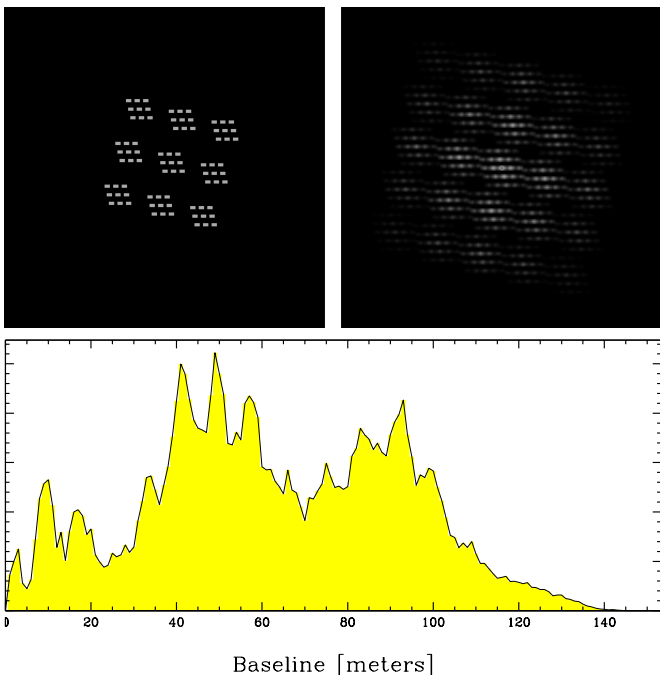


FIG. 2: The antenna layout (top left) from Figure 1 convolved with its parity reversal gives the two-dimensional baseline distribution (top right), and binning this radially gives the one-dimensional baseline distribution (bottom), which is plotted on a linear scale. The layout corresponds to $\mathbf{a}_1 = (1, 0)$, $\mathbf{a}_2 = (8, 0)$, $\mathbf{a}_3 = (40, 10)$, $\mathbf{a}_4 = (0, 1)$, $\mathbf{a}_5 = (2, 8)$, $\mathbf{a}_6 = (-10, 40)$, $n_1 = 1, \dots, 5$ and n_2 through n_6 all ranging from 1 to 3.

scales as N^2 : these are 500-tile simulations described in [20] for the MWA-experiment, using random antenna placements with a radial density scaling as r^0 (uniform), r^{-1} , r^{-2} and r^{-3} , respectively. The r^{-2} example is illustrated in 2D in Figure 6. When plotting the 2D baseline distribution d , we convolved the layout map l with its parity reversal, $d = l \star l^-$, where the layout map just contains one in every entry. We have zeroed the origin and chosen a grey-scale where the intensity is proportional to $\sinh^{-1}(4d/d_{\max})$ to avoid saturation and allow decent legibility at both small and large values of d . Note that the different examples have a different total number of antennas.

In Appendix A, we will discuss the issue of how these baseline distributions can be filled in by exploiting Earth rotation. For our present discussion, we will focus on radially binned versions of these baseline distributions, which show how much information is measured on different angular scales.

The first point illustrated by these examples is that a wide variety baseline distributions can be achieved with a hierarchical antenna grid — which is hardly surprising given how large this class of grids is. Figure 7 compares the four hierarchical grid examples (bottom panel) with the four simulated MWA examples (top panel), all rescaled to have a 1 km maximum baseline. Because our different examples have different number of antennas, the curves have been arbitrarily rescaled in the vertical di-

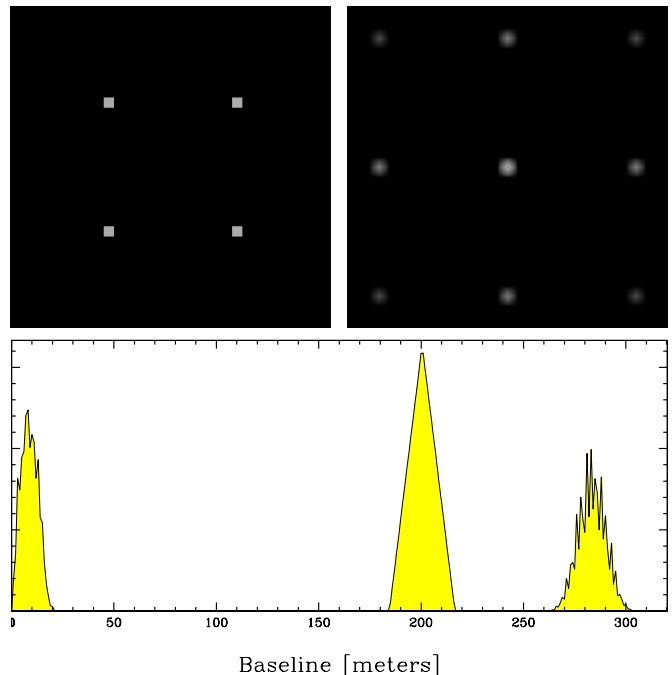


FIG. 3: Antenna layout (top left), 2D baseline distribution (top right) and 1D baseline distribution (bottom) for the hierarchical “Blocks” layout consisting of four widely separated 16×16 antenna blocks ($\mathbf{a}_1 = (1, 0)$, $\mathbf{a}_2 = (200, 0)$, $\mathbf{a}_3 = (0, 1)$, $\mathbf{a}_4 = (0, 200)$, $n_1 = n_3 = 16$, $n_2 = n_4 = 2$).

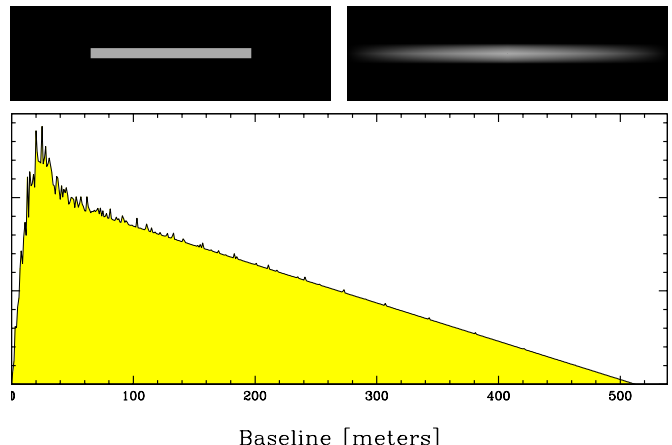


FIG. 4: Antenna layout (top left), 2D baseline distribution (top right) and 1D baseline distribution (bottom) for the “Plank” layout consisting of a single 512×32 antenna block. ($\mathbf{a}_1 = (1, 0)$, $\mathbf{a}_2 = (0, 1)$, $n_1 = 512$, $n_2 = 32$).

rection for legibility. Thus only the shapes of the plotted curves are important, not the amplitudes. We see that if one has a preference for one of these MWA-distributions, then faster-to-analyze hierarchical grids can reproduce at least some of their broad-brush features: note the similarities between “ r^{-2} ” and “Plank”, and between “Uniform” and “Strips”.

In addition, we see that hierarchical grids can easily offer quite different types of baseline distributions as well. For example, “Blocks” is seen to provide sensitivity on widely separated angular scales, which may be desirable.

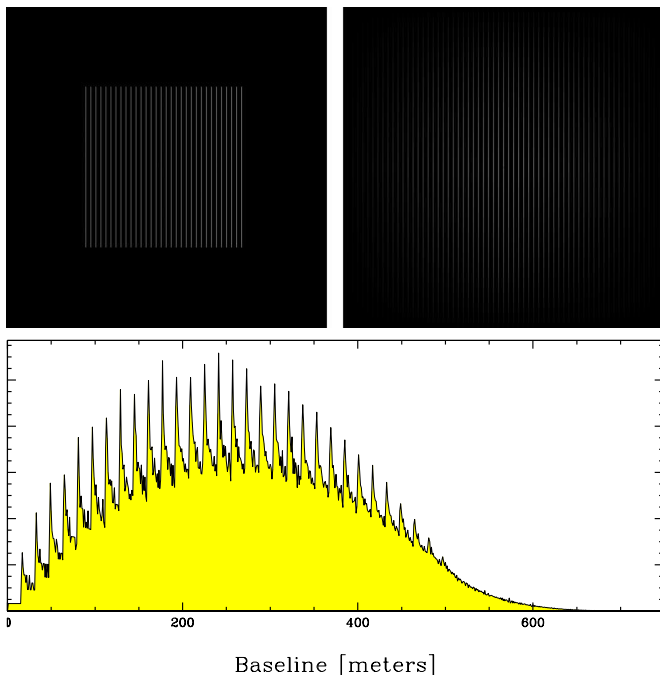


FIG. 5: Antenna layout (top left), 2D baseline distribution (top right) and 1D baseline distribution (bottom) for the “Strips” layout consisting of 32 separated rows of antennas ($\mathbf{a}_1 = (16, 0)$, $\mathbf{a}_2 = (0, 1)$, $n_1 = 32$, $n_2 = 512$).

able for some science applications (like 21cm tomography, where short baselines are needed to probe the cosmological signal and long baselines are needed for point source removal).

If one drops the requirement of strictly optimal ($N \log N$) computational cost and is willing to stomach an extra factor of two, then building a second completely separate omniscopes can offer interesting advantages. For example, if two omniscopes with the “Plank” layout of Figure 4 are built rotated by 90° relative to one another, then full rotation synthesis can be obtained in merely 6 hours instead of 12, conveniently carried out during a single night. Note that in this way, one computes only correlations within each “Plank” and as a result the one gathers just half the available information. Even if daytime observations are acceptable, this greatly improves the uv coverage in generic sky directions from generic latitudes. In the limit where the width of the Plank shrinks to a single antenna, this is similar in spirit to the cylinder telescopes designed by [16, 17]. (Note that if two cylinders are not parallel (as in the Mills Cross telescope [21]), then correlation obviously requires the full N^2 cost, since there are $\sim N^2$ separate baselines to compute.)

In the same spirit, another interesting variant [22, 23] is to use FFT-correlation separately in a set of (M/N) different rectangular sub-arrays (“tiles”) of M antennas each that are translated relative to each other by arbitrary amounts, and correlate the corresponding synthesized beams between tiles using the brute-force $(N/M)^2$ approach, giving a total computational cost of $(M \log M)(N/M)^2 \sim (N \log N)(N/M)$. This is an in-

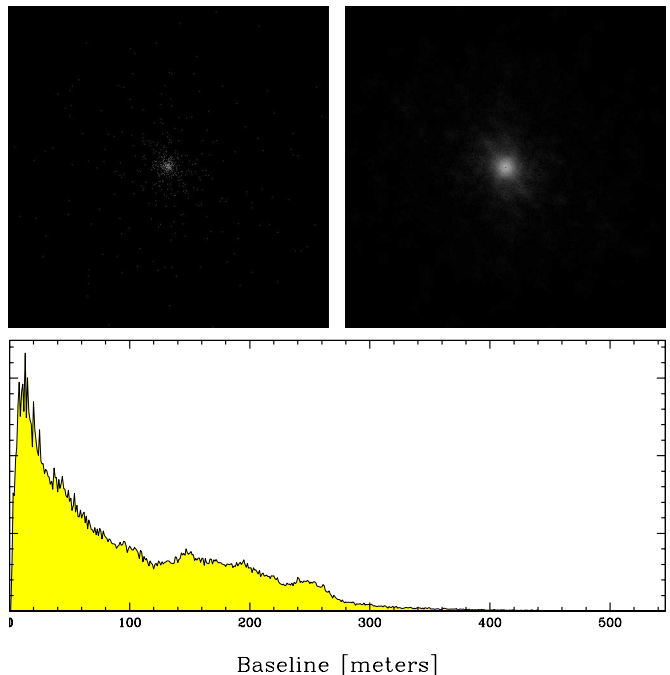


FIG. 6: Antenna layout (top left), 2D baseline distribution (top right) and 1D baseline distribution (bottom) for a the simulated MWA design from [20] with r^{-2} antenna density.

termediate case cheaper than the straight N^2 and more expensive than an $N \log N$ omniscopes because it exploits the FFT speedup for two hypercube dimensions, within but not between tiles.

Our examples above assumed no errors in the antenna positions relative to the hierarchical grid. The question of how antenna position errors affect calibration and image reconstruction deserves further work. A first exploration of this problem can be found in [24], showing how calibration errors scale linearly with such position errors, and how this scaling can be improved to quadratic or better with more elaborate software.

IV. CONCLUSIONS

We have shown that the class of antenna layouts for radio telescope arrays allowing cheap analysis hardware (with correlator cost scaling as $N \log N$ rather than N^2 with the number of antennas N) is encouragingly large, including not only previously discussed rectangular grids but also arbitrary hierarchies of such grids, with arbitrary rotations and shears at each level.

This hierarchical grid layout can allow major correlator cost reductions for science applications requiring sensitivity at widely separated angular scales, for example 21 cm tomography (where short baselines are needed to probe the cosmological signal and long baselines are needed for point source removal). For example, the computers for calculating the $\sim N^2$ correlations constitute (by design) about half the hardware cost of the 512-element MWA telescope [8], so for the significantly larger N -values that

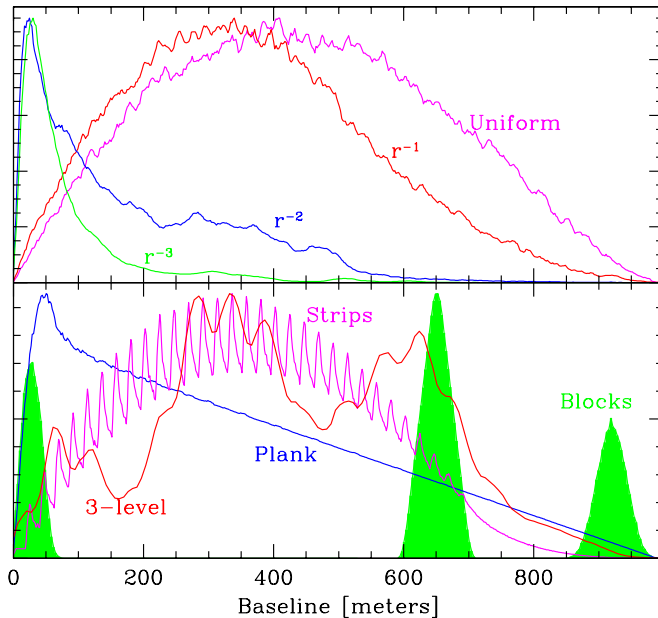


FIG. 7: The baseline distributions from four simulated MWA layouts with N^2 computational cost (top) are compared with baseline distributions from four hierarchical grids with $N \log N$ computational cost (bottom). For improved legibility, all curves in this figure have been boxcar smoothed with a sliding bin of width 5 meters to reduce noise.

will be needed to perform precision 21 cm cosmology [5–7], computing hardware will completely dominate the budget of any non-hierarchical array. Looking towards a future with more sensitive instruments, hierarchical grids can therefore be used both to cut the costs for a fixed collecting area and to boost the area attainable with a given budget.

If a science goal requires a good approximation to a particular baseline distribution (in 1D or 2D), one can use simulated annealing or another suitable tool to solve the nonlinear optimization problem of where to place the antennas, either within the hierarchical grid class of layouts or with complete freedom. In most cases, general non-hierarchical grids can obviously provide the most accurate approximation, but at a much higher price. It is therefore worthwhile to start paying closer attention to what baseline distributions one actually needs for various science applications, and to quantify whether the case for non-hierarchical layouts is compelling enough to justify the extra cost. By definition, a hierarchical grid will fill a smaller fraction of the uv plane per snapshot (concentrating all its sensitivity measuring or order N rather N^2 baselines), but as described in Appendix A, this can in many cases be made up for by rotation synthesis. Moreover, the massive uv redundancy, whereby most baselines are independently measured by many antenna pairs, offers a powerful tool for internal calibration and systematic error control of an omniscopes. In [24], it is shown

with detailed simulations that such calibration based on redundant baselines calibration with an omniscopes can be made both accurate and computationally feasible.²

In summary, there is now strong community interest in building more sensitive radio arrays consisting of large numbers of cheap dipole-like antennas, and our results indicate a potential for doing so with more bang for the buck.

Acknowledgements: The authors wishes to thank Adrian Liu, Andy Lutomirski and anonymous referees for helpful comments, and Adrian Liu and Judd Bowman for providing simulated MWA antenna distributions. This work was supported by NASA grants NAG5-11099 and NNG 05G40G, NSF grants AST-0607597, AST-0708534, AST-0908848 and PHY-0855425, and fellowships from the David and Lucile Packard Foundation and the Research Corporation.

² Our examples in Section III assumed no errors in the antenna positions relative to the hierarchical grid. The question of how antenna position errors affect calibration and image reconstruction deserves further work. A first exploration of this problem can be found in [24], showing how calibration errors scale linearly with such position errors, and how this scaling can be improved to quadratic or better with more elaborate software. There are also a number of issues for which the FFT-based correlation does no better and no worse than traditional N^2 correlation; once the baseline distribution is fixed, our hypercube algorithm is after all just a mathematical trick for computing the exact same numbers as with the N^2 method, just faster. Such issues include sidelobes due to spatial undersampling, ionospheric modeling [25–27], and direction-dependent gain calibration. The first can be mitigated by planing antennas less than a wavelength apart at the lowest level of the hierarchical grid. The above-mentioned redundancy can help also with direction-dependent gain calibration if there are point sources with known positions that completely dominate the signal in their frequency band (like the ORBCOMM satellites), and for the wavelengths most relevant to 21cm tomography, the ionosphere only becomes a problem for baselines above the kilometer scale.

Appendix A: Rotation synthesis and mapmaking with hierarchical omniscopes

Above we described how a hierarchical omniscopes could be correlated at an $N \log N$ computational cost per snapshot. In this Appendix, we will discuss how, in the spirit of the standard radio-astronomy technique known as faceting [19], such snapshots can be combined into a seamless sky map with minimal noise and a well-characterized synthesized beam, again at a modest computational cost.

1. Optimal mapmaking

The theory of how to make maps with minimal noise has been extensively developed and applied in the context of CMB observations (see for example [28])³. Consider a set of n observations which we arrange in a vector \mathbf{y} (in our case these are the measured correlations, $N(N-1)/2$ visibilities per snapshot in time). We will assume that \mathbf{y} is of the form

$$\mathbf{y} = \mathbf{A}\mathbf{x} + \mathbf{n}, \quad (\text{A1})$$

where \mathbf{x} is an m -dimensional vector with the intensity (and polarization) of the sky in different directions, \mathbf{A} is a known matrix encoding the response of the instrument and \mathbf{n} is the noise. Our goal is to recover \mathbf{x} in a way that does not lose any of the cosmological information. There are many possible linear lossless estimators of \mathbf{x} , because if one multiplies any lossless estimator by an invertible matrix, the resulting vector also contains all the available information. As discussed in [28], these lossless estimators are of the form

$$\hat{\mathbf{x}} = \mathbf{M}\mathbf{A}^t\mathbf{N}^{-1}\mathbf{y}, \quad (\text{A2})$$

where \mathbf{M} is an $m \times m$ matrix. A possible choice of \mathbf{M} is $\mathbf{M} = [\mathbf{A}^t\mathbf{N}^{-1}\mathbf{A}]^{-1}$ which makes the estimator \mathbf{x} unbiased, but there are also other popular choices with different attractive features. Note that $\hat{\mathbf{x}}$ has size m , the size of the pixelized sky map. The \mathbf{y} -vector contains all the observed visibilities and thus in general has a size much greater than m . The multiplication by \mathbf{A}^t is the step that accumulates or bins the observations into a single map. Equation A2 constitutes a form of lossless data compression.

2. The key challenge: rapid multiplication by \mathbf{A}^t

For the purpose of our discussion, the crucial point is being able to compute $\hat{\mathbf{x}}$ or a good approximation to it

fast, in no more than of order $N \log N$ operations which is what is needed to compute all the correlations in \mathbf{y} . If we assume that the noise in each visibility is uncorrelated, then the noise matrix \mathbf{N} is diagonal and multiplying by \mathbf{N}^{-1} is computationally cheap. The key challenge is then being able to apply \mathbf{A}^t to the data in an efficient way. This requires that \mathbf{A} be a sufficiently sparse matrix⁴. Of course one has the choice of representing the vector \mathbf{x} in any basis, for example one could pixelize the sky in a standard fashion with one pixel per direction on the sky or one could represent the sky by its Fourier modes. The same is true for \mathbf{y} . We will attempt to exploit this freedom to choose a basis in which \mathbf{A} is maximally sparse. For simplicity, we will discuss only the unpolarized case below, as polarization does not change the problem in any fundamental way.

a. The problem with real space

The most straightforward choice would be pixelize the sky in angular space, with each entry in \mathbf{x} corresponding to a different direction in the sky. For a given snapshot, a row in \mathbf{A} then combines the intensity on the sky to give the response of a visibility, while each row of \mathbf{A}^t combines all the visibilities into an estimate of the sky in a given direction. Defined in this way, \mathbf{A}^t is not sparse or compact because visibilities have response everywhere within the primary beam.

We can improve the situation by changing basis for \mathbf{y} . We could use an FFT to go from the measured visibilities in the uv plane to angle space (what is usually referred to as the “dirty map” in the radio astronomy literature) in $N \log N$ operations. Now both \mathbf{y} and \mathbf{x} are in angle space. With this choice, the matrix \mathbf{A} is nothing but what is usually called the instantaneous synthesized beam of the interferometer (the Fourier transform of the 2D baseline distributions shown in the top right panels of Figures 2-6). Unfortunately, for generic array layouts, the instantaneous synthesized beam tends to be quite complicated, with important side lobe structure, positive and negative regions, *etc.* Although better than before, the \mathbf{A} matrix is therefore still not very compact, so multiplying the data by \mathbf{A}^t would dominate the computational costs, spoiling the advantage of the omniscopes design.

³ For a discussion of the related topic of how to go straight from snapshots to power spectrum estimates, see [29]

⁴ We will assume that one can also multiply by the \mathbf{M} -matrix sufficiently fast; this can often be done with an iterative approach once the \mathbf{A}^t -multiplication is rapid, as successfully demonstrated by the WMAP team for their microwave background analysis[31].

b. *The problem with Fourier space*

If the omniscopes are located at the South Pole, then what to do is rather trivial: one simply aggregates all correlation measurements in a single uv plane. That is to say, we use the Fourier basis to describe \mathbf{x} . For each snapshot in time, an observed visibility is the convolution of the Fourier transform of the sky with the Fourier transform of the primary beam. The baselines probed by each antenna pair simply rotates with Earth. In this case, the entries of the \mathbf{A} matrix are given by the Fourier transform of the primary beam, which can be made very compact, so the \mathbf{A}^t multiplication is computationally cheap. One accumulates the observations in the uv plane, and after 12 hours, one can then Fourier transform the resulting intensity to recover a map of the Southern half of the sky in an easy-to-interpret projection [18]. Fourier transforming the corresponding uv weight map recovers the effective synthesized beam.

Unfortunately, for a general array layout, it is well-known that there are no easy solutions for mapping a large solid angle [19], because of the complication that the plane of the array rotates over time. One cannot simply accumulate observations in the same uv plane. Although instantaneously the uv plane is clearly the best choice, the uv plane is defined relative to the interferometer rather than fixed to the sky, so it is not a good basis to parametrize the sky once long observations are involved.

c. *A solution: multiple uv planes*

There is, however, a class of omniscopes designs for which the global mapping problem can be easily solved for an arbitrary observing location on Earth: the case of a hierarchical grid where the lowest level of the hierarchy consists of square $n \times n$ antenna blocks that are fully sampled (with the individual antennas of order a wavelength apart). If each of these blocks is operated as a phased array, they can all be digitally pointed to a generic point $\hat{\mathbf{r}}$ in the sky and will be sensitive only to signals from within about an angle $\Delta\theta \sim 1/n$ around this point. As long as $n \gg 1$, the flat sky approximation can be used for this patch of sky, and one can use standard radio astronomy procedures to combine all digital pointings towards that sky patch in a uv plane defined as the Fourier dual of the tangent plane to $\hat{\mathbf{r}}$ (extended of order $\Delta\theta$ around $\hat{\mathbf{r}}$). Note that in this way, the uv plane fixed to the sky rather than to the plane of the instrument, and is used to represent a small patch.

With an omniscopes consisting of many such $n \times n$ blocks, one can follow exactly the same procedure, except that one simultaneously obtains n^2 different pointings of the antenna blocks. In practice one would divide the sky into a number of small patches (“facets”) over which the flat sky approximation is valid and use the Fourier basis to describe the intensity in each patch. Each of the pointings of the omniscopes would then be assigned to the

uv plane of one of these patches.

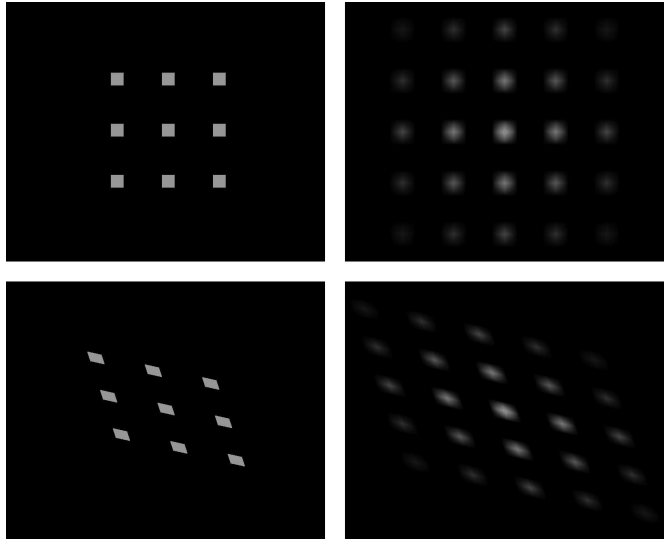


FIG. 8: The antenna layout (top left) and 2D baseline distribution (top right) of nine 40×40 antenna blocks appear deformed (bottom panel) when viewed from a sky direction other than the zenith (here the elevation is 30° and the azimuth is 63°).

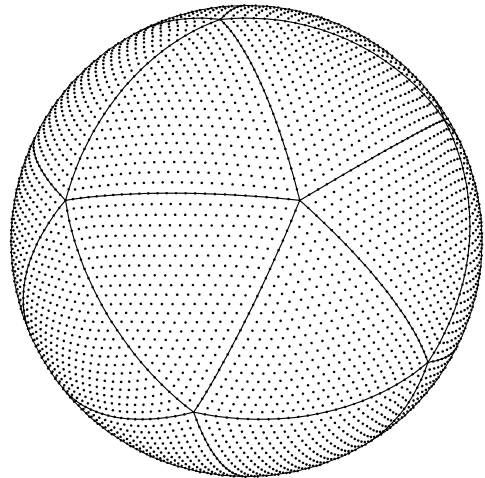


FIG. 9: To make the flat sky approximation as accurate as possible within a fixed number of pixels, it is helpful to make the pixels hexagonal as in this equal-area icosahedron-based scheme [30] (the pixel centers are shown as dots).

As an illustration, consider the following specific example. We have nine $n \times n$ antenna blocks with $n = 40$, arranged as in Figure 8. Since the primary beam size of each such block will be a few degrees, we partition the sky into 6252 hexagonal pixels of roughly this size using the pixelization method of [30] as illustrated in Figure 9: each point in the figure corresponds to a pixel center, and each point (unit vector $\hat{\mathbf{r}}$) belongs to the pixel whose center it is closest to. This makes generic pixels hexagonal, which has the advantage of minimizing sky curvature

effects [30]. For each pixel center, we keep track of an associated uv plane. Note that the sky pixelization is fixed in the sense that it does not change as the Earth rotates. We now process the omniscopes data as follows:

1. Collect data for say 1 second.
2. FFT the data from each antenna in the time domain and calibrate as necessary.
3. For a given frequency bin, arrange the data in a hypercube as in Section II.
4. Perform a two-dimensional FFT for each of the blocks, thereby obtaining digital pointings in 32×32 different sky directions $\hat{\mathbf{r}}_i$, $i = 1, \dots, 1024$.
5. Perform the correlation in all remaining dimensions using a pair of FFT's as in Section II.
6. Merge the data from each such pointing $\hat{\mathbf{r}}_i$ into the uv plane corresponding to the closest pixel center, bearing in mind that the baseline distribution must be appropriately rotated and shortened by a factor $\cos \theta \equiv \hat{\mathbf{z}} \cdot \hat{\mathbf{r}}_i$ to reflect the way the array looks viewed from the direction $\hat{\mathbf{r}}_i$, and that the polarization vector must be correspondingly rotated. The phases must also be adjusted to reflect the translation from each pixel center to $\hat{\mathbf{r}}_i$. For the pointing direction $\hat{\mathbf{r}}_i$ from which the array looks deformed like in Figure 8 (bottom left), the corresponding uv weight function thus gets augmented by the corresponding deformed baseline distribution (bottom right).
7. Repeat for all frequency bins of interest.
8. Repeat for as long an integration as desired, exploiting that the pointing directions $\hat{\mathbf{r}}_i$ in celestial coordinates rotate with Earth.
9. FFT the data in each of the 6252 uv planes to obtain maps of the corresponding sky patches, and FFT the corresponding uv weight functions to obtain the corresponding synthesized beam functions.
10. Seamlessly merge all the patches into a single map.

It is interesting to compare this approach (for observations in a single uv plane) with what [32] term “software holography”. The similarity is that in both cases, each measured visibility is accumulated in the uv -plane not as a delta function (by adding the measured complex number to a single uv pixel), but rather as the Fourier transform of the instantaneous primary beam (corrected for deformation and translation as in Figure 8), adding in this uv image multiplied by the measured complex number. In both cases, it is important that the uv plane where the visibilities and weight functions are accumulated are well oversampled, to adequately resolve the

antenna shapes. The difference is that software holography does this operation once for every sample (say once every nanosecond), whereas with our omniscopes approach it is sufficient to do this only once per snapshot (say every second). This omniscopes approach thus enables major computational savings, since all that needs to happen for every sample is the much simpler FFT-processing, where no oversampling is needed and each measured number is inserted in only one place (in the hypercube).

Perhaps the only subtlety in the omniscopes mapmaking algorithm above relates to the splitting of the sky into domains and the combination of the different domains into a single final map. In particular, a given pointing of the omniscopes could land on the boundary between domains. We can treat this by making the domains overlap as follows. First write

$$\mathbf{y} = \mathbf{A}\mathbf{x} + \mathbf{n} \equiv \mathbf{P}\mathbf{D}\mathbf{x} + \mathbf{n}, \quad (\text{A3})$$

where we have decomposed the \mathbf{A} matrix into several pieces. First \mathbf{D} splits the sky into domains. Note that we can decide to assign each pixel on the sky to more than one domain. For example we can choose to make the domains overlap in such a way that whenever the center of a pointing of the omniscopes falls in one domain, we will assign the entire primary beam to that domain. As a result, the domains will have to overlap as a pointing whose center is near the edge of a domain “spill” into neighboring ones. Rather than assigning measurements of each pointing to more than one patch, we simply make the patches overlap and assign each pointing to only one patch. As a result the \mathbf{D} -matrix is not a square matrix. If for example we choose to have each pixel on the sky belong to three domains, \mathbf{D} is a $3m \times m$ matrix. The matrix \mathbf{F} simply changes basis to describe the intensity in each domain by its Fourier transform, that is to say it goes from angle space to the uv plane. Finally, each visibility is given by the convolution of the Fourier modes in a given patch with the primary beam of the tile, encoded in the matrix \mathbf{P} . As described above, the projected separation of each pair of antennas and the location of the center of the pointing relative to the center of the sky patch are needed to compute \mathbf{P} . Note also that the size and shape of the primary beam also depends on the direction of the pointing.

Now the estimate of the sky becomes

$$\hat{\mathbf{x}} = \mathbf{M}\mathbf{D}^t\mathbf{F}^t\mathbf{P}^t\mathbf{N}^{-1}\mathbf{y}, \quad (\text{A4})$$

where \mathbf{P}^t accumulates the visibility measurements in the individual uv planes fixed to the sky. After all the measurements were accumulated in each domain, \mathbf{F}^t goes back to angle space from Fourier space. Finally, \mathbf{D}^t combines the measurements in all the domains into a single sky map.

-
- [1] C. Carilli and S. Rawlings eds., *Science with the Square Kilometre Array* (Elsevier: Amsterdam, http://www.skads-eu.org/p/SKA_SciBook.php, 2004)
- [2] R. Barkana and A. Loeb, *ApJL*, **624**, L65 (2005)
- [3] J. D. Bowman, M. F. Morales, and J. N. Hewitt, *ApJ*, **661**, 1 (2007)
- [4] M. McQuinn, O. Zahn, M. Zaldarriaga, L. Hernquist, and S. R. Furlanetto, *ApJ*, **653**, 815 (2006)
- [5] Y. Mao, M. Tegmark, M. McQuinn, O. Zahn, and M. Zaldarriaga, *PRD*, **78**, 023529 (2008)
- [6] A. Loeb and S. Wyithe, *PRL*, **100**, 161301 (2008)
- [7] V. Barger, Y. Gao, Y. Mao, and D. Marfatia, *PLB*, **673**, 173 (2009)
- [8] MWA: <http://www.haystack.mit.edu/ast/arrays/mwa/>
- [9] LOFAR: <http://www.lofar.org/>
- [10] A. R. Parsons, arXiv:0904.2334 (2009)
- [11] <http://web.phys.cmu.edu/~past/>, formerly known as *PaST*.
- [12] J. Butler and Lowe R., *Electronic Design*, **9**, 170-173 (1961)
- [13] J. May, F. Reyes, J. Aparici, M. Bitran, H. Alvarez, and F. Olmos, *A&A*, **140**, 377 (1984)
- [14] J. Nakajima *et al.*, *PASJ*, **44L**, 35 (1993)
- [15] J. Nakajima *et al.*, *PASJ*, **45**, 477 (1993)
- [16] J. B. Peterson, K. Bandura, and U. L. Pen, astro-ph/0606104 (2006)
- [17] T. Chang, U. Pen, J. B. Peterson, and P. McDonald, *PRL*, **100**, 091303 (2008)
- [18] M. Tegmark and M. Zaldarriaga, *PRD*, **79**, 083530 (2009)
- [19] A. R. Thompson and J. M. Moran, and G. W. Swenson, *Interferometry and Synthesis in Radio Astronomy, 2nd Ed.* (Wiley: New York, 2001)
- [20] J. D. Bowman, M. F. Morales, and J. N. Hewitt, *ApJ*, **661**, 1 (2007)
- [21] B. Burke, *Astron. J*, **61**, 167 (1956)
- [22] J. D. Bunton, T. Joseph, and W. Lazio, *Experimental Astronomy*, **17**, 417 (2004)
- [23] U. Pen, *New Astron.*, **9**, 417 (2004)
- [24] A. Liu, M. Tegmark, S. Morrison, and A. Lutomirski, arXiv:1001.5268 (2010)
- [25] A. S. Cohen and H. J. A Röttgering, *Astron.J*, **138**, 439 (2009)
- [26] M. S. Matejek and M. F. Morales, arXiv:0911.3942 (2009)
- [27] L. V. E Koopmans, arXiv:1005.1898 (2010)
- [28] M. Tegmark, *ApJ*, **480**, L87 (1997)
- [29] E. F. Bunn and M. White, *ApJ*, **655**, 21 (2007)
- [30] M. Tegmark, *ApJL*, **470**, L81 (1996)
- [31] G. Hinshaw *et al.*, *ApJS*, **148**, 63 (2003)
- [32] M. F. Morales and M. Matejek, *MNRAS*, **400**, 1814 (2009)